Ore Geology Reviews 185 (2025) 106799

Contents lists available at ScienceDirect

Ore Geology Reviews

journal homepage: www.elsevier.com/locate/oregeorev

Nanoscale study of Fe-Mn micronodules in deep-sea sediment from the Western Pacific Ocean

Yaqin Wang [a], Lei Zuo [a], Peng Zhang [a], Ming Su [b,c], Yuzhi Xu [a,*], Rui Liu [a,*], José María González-Jiménez [d], Fernando Gervilla [d,e]

[a] School of Resources and Environmental Engineering, Shandong University of Technology, Zibo 255000, China
[b] School of Marine Sciences, Sun Yat-Sen University, Zhuhai 519082, China
[c] Guangdong Provincial Key Laboratory of Marine Resources and Coastal Engineering, Zhuhai 519082, China
[d] Instituto Andaluz de Ciencias de la Tierra (IACT), CSIC-UGR, Avda. de las Palmeras 4, 18100 Armilla Granada, Spain
[e] Departamento de Mineralogiay Petrologia, Facultad de Ciencias, Universidad de Granada, Avda Fuentenueva s/n, 18002 Granada, Spain

ARTICLE INFO

Keywords:
Nanoparticle
The Western Pacific
Fe-Mn micronodule
Elemental correlation
Early growth process

ABSTRACT

This study collected early-stage Fe-Mn micronodules from the seafloor of the Western Pacific and analyzed their structural characteristics and elemental distribution using Scanning Electron Microscopy (SEM), Focused Ion Beam (FIB) and Transmission Electron Microscopy-Energy Dispersive X-ray Spectroscopy (TEM-EDS). The results indicate that the micronodule exhibits stratified growth profiles, including laminated structures, lamellar structures and porous loose layers. Fe and Ti are concentrated in the core region of the micronodule, followed by a clay mineral layer enriched in Al, Mg, Si and K, while the outermost layer is dominated by Mn, forming a dense layer enriched with I and Pb at the edge. The distribution of Fe and Mn within the micronodule shows a clear negative correlation. Further analysis revealed that the main mineral phases in the micronodule (ferrihydrite and montmorillonite), as well as the titanium oxides, manganese oxides and lead iodide located at the edge of the micronodule, all exist as nanoparticles. Ferrihydrite is positively correlated with the enrichment of heavy rare earth elements (HREEs) such as Dy, Tb, Er and Tm, while manganese oxides play a significant role in the selective removal or enrichment of specific light rare earth element (LREE) like Eu, as well as certain HREEs such as Er, Tm and Gd. Additionally, the presence of Ti, clay minerals, I and Pb may have a critical influence on the enrichment of Tm, Er, Gd, Yb, Ho, Ce, Pr, La, Nd, Sm, K and Mg in the regional marine environment. These findings enhance our understanding of the mechanisms governing the occurrence and distribution of rare earth elements (REEs) in Fe-Mn micronodules and highlight the pivotal role of nanoparticles in the early-stage growth and elemental enrichment of micronodules, providing new insights into the genesis and evolution of deep-sea Fe-Mn micronodules.

1. Introduction

The deep-sea sedimentary environment fosters a variety of metal-rich mineral resources. Among these, Fe-Mn micronodules, as important carriers of REEs and trace metals in marine sediments, have attracted increasing attention (Menendez et al., 2017). Compared to the more widely known centimeter-scale nodules, micronodules possess a much higher specific surface area but are mineralogically and morphologically similar to large nodules (Dubinin and Sval'nov, 2000a; Dubinin and Sval'nov, 2000b; Dubinin et al., 2017). They are primarily composed of iron and manganese oxides and contain a variety of critical metals such as Fe, Mn, Ni, Cu, Mo, Li, Co and REEs (Glasby et al., 1978; Halbach et al., 1981; Hein and Koschinsky, 2013; Bau et al., 2014; Hein et al., 2015; Xu and Zhou, 2022). Fe-Mn nodules and micronodules are widely distributed on deep-sea plains, abyssal basins and sediment-covered seamounts (Yin et al., 2019), with global seabed reserves estimated at approximately 3 trillion tons, of which the Pacific Ocean accounts for roughly 1.7 trillion tons (Niu, 2002). Micronodules, in particular, are distributed over a much greater area than their larger counterparts and have thus become a potentially significant source of strategic metals such as REEs (Kato et al., 2011; Dekov et al., 2021).

For a long time, due to their finer grain size, lower economic benefit

* Corresponding authors.
E-mail addresses: xuyuzhi@sdut.edu.cn (Y. Xu), liurui@sdut.edu.cn (R. Liu).

https://doi.org/10.1016/j.oregeorev.2025.106799
Received 3 March 2025; Received in revised form 16 July 2025; Accepted 20 July 2025
Available online 21 July 2025

and the greater difficulty associated with separation and detection, the geological and resource value of Fe-Mn micronodules has been relatively overlooked (Addy, 1979; Dekov et al., 2003). However, recent studies provide increasing evidence that micronodules exhibit pronounced enrichment of REEs, primarily attributed to their high porosity and the strong adsorptive properties of Fe-Mn (hydr) oxides (Zhang et al., 2023a). For instance, Menendez et al. (2017) documented ΣREY concentrations up to 3620 ppm in micronodules, an order of magnitude higher than surrounding sediments. Therefore, their economic and scientific potential warrants further comprehensive evaluation.

Fe-Mn micronodules typically form in deep-sea basins characterized by low sedimentation rates, moderate to low biological productivity and oxidizing conditions. During their formation, Fe^{2+} and Mn^{2+} are oxidized and precipitated onto the surfaces of sediment particles (Glasby et al., 1978; Winter et al., 1997; Hein et al., 2015; Dubinin et al., 2013, 2017; Liao et al., 2019). Even though the overall oxygen content in deep-sea basins or abyssal plains is generally low, localized oxidizing environments created by ocean currents are sufficient to facilitate the formation of these metal-rich micronodules (Wu et al., 2022; Luo et al., 2023). Unlike macroscopic nodules, which often exhibit distinct Fe-Mn banding (Von Stackelberg, 1997; Ohta et al., 1999), micronodules display more continuous internal growth sequences (Liao et al., 2019) and possess a complex mineralogical composition comprising various Fe-Mn minerals, such as vernadite, todorokite, buserite, birnessite, feroxyhyte and goethite. Additionally, they are commonly associated with clay minerals (montmorillonite, illite) and with detrital quartz (Usui and Someya, 1997; Post, 1999; Du and Lv, 2003; Guan et al., 2019; Liao et al., 2019; Xu et al., 2024a). The outer layers of micronodules are typically enriched in Mn, Co, Ni, Cu and REEs, whereas the cores are dominated by Fe, Al, K and Si, reflecting a close relationship between the mineral assemblage and the environmental conditions of formation (Wu et al., 2022; Liao et al., 2019). Some researchers have suggested that the growth layers of micronodules may record fluctuations of the oxic-suboxic boundary within the sediment column (Dekov et al., 2021).

Despite significant progress, studies on the nanoscale structure, elemental distribution characteristics and enrichment processes during the early-stage growth of Fe-Mn micronodules remain insufficient. On the one hand, the extremely fine grain size and poorly ordered crystal structure of micronodules make it difficult for conventional chemical and mineralogical analyses to resolve their nanoscale features (Addy, 1979; Menendez et al., 2017). On the other hand, mineral phase transformations and elemental re-equilibration during prolonged geological processes may obscure the original depositional characteristics (Guan et al., 2017; Ren et al., 2023; Lee et al., 2019; Liao et al., 2019). Therefore, there remain clear gaps with respect to critical scientific questions such as the nanoscale structural characteristics, elemental enrichment patterns and constituent distribution features of micronodules during their early growth stage.

To address these gaps, this study investigates Fe-Mn micronodules collected from the Kyushu-Palau Ridge in the Western Pacific Ocean, with a focus on elucidating their nanoscale structure, elemental distribution characteristics and enrichment processes during the early growth stage. By integrating SEM, FIB and TEM techniques, we systematically analyze the microstructure and local composition of micronodules, providing an important foundation for subsequent studies on their resource potential and genetic models.

2. Samples and methods

2.1. Samples

Deep sea sediment samples were collected from the site XT25 in the east part of the west Philippine Basin (15.32 °N, 133.23 °E) near the Kyushu-Palau Ridge of the Weste Pacific Ocean in June 2018 (Fig. 1). The deposition rate near the sampling point is slow, about 142 cm/Myr (Hu et al., 2021). The West Philippine Basin is the world's largest marginal basin plate. It was formed during the Paleocene undersea expansion activity and surrounded by subduction boundaries. The area is characterized by a subtropical East Asian monsoonal climate (Wan et al., 2012). The deep-sea water in the basin is primarily influenced by the lower circumpolar deep water (LCDW; Kawabe and Fujio, 2010), with annual sea surface temperatures averaging 28.5 °C and salinity at 34.43 practical salinity unit (psu; Yan et al., 1992; Mohtar et al., 2021). The geological setting of the West Philippine Basin is unique, featuring a complex crustal structure situated between the Pacific, Eurasian and Australian plates. The North Equatorial Current and the Kuroshio Current are the most significant oceanographic currents in the area (Lin et al., 2021). The North Equatorial Current serves as a crucial pathway for zonal heat and water mass exchange across the tropical Pacific Ocean (Qiu et al., 2014). The sampling site was at a water depth of 4941.9 m. The sediment core, collected using a gravity corer, had a recovered length of 4 m and a diameter of 0.1 m. The samples were immediately stored in sterile polypropylene containers and frozen at −20 °C. Upon returning to the laboratory, all samples were subsequently frozen at −80 °C.

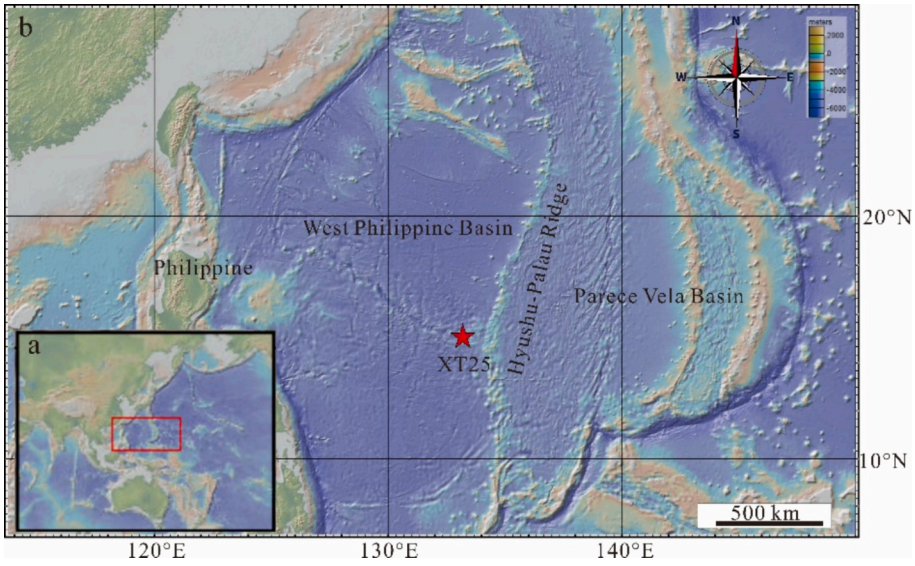

Fig. 1. Location map of deep-sea sediment sample collection (USCGS, 2013).

2.2. Methods

The major and trace element compositions of the sediments were first analyzed at ALS Chemex Co., Ltd. (Guangzhou), using X-ray fluorescence spectrometry (XRF) and a Thermo Fisher iCAP Qc inductively coupled plasma mass spectrometer (ICP-MS), respectively. The results are presented in Table S1. Subsequently, all microstructural characterization and microscale compositional analyses were conducted at Sinoma Institute of Materials Research (Guangzhou) Co. Ltd./SinomaTest (Guangzhou) Co. Ltd. After determining the major and trace elements, the sediment samples were vacuum-dried, then a small amount was dispersed on conductive adhesive and fixed onto the SEM sample stage. The samples were gently compacted to ensure stability and electrical contact. Subsequently, preliminary morphological observation and photography of the sediment samples were conducted, during which micronodules were identified. To facilitate subsequent FIB sampling and TEM analysis, micro-nodules were progressively screened under low-magnification and high-magnification SEM images after sample fixation, followed by further micro-area analysis. Initial morphological examination was performed using a Hitachi SU8220 SEM at accelerating voltages of 5 kV and 10 kV to ensure clear imaging of the sample surfaces. To achieve higher resolution and better contrast, additional imaging was performed using a Zeiss SEM at an accelerating voltage of 20 kV and a working distance (WD) of approximately 8.5–8.6 mm in backscattered electron (BSE) mode (Signal A = HDAsB). Typical magnifications ranged from approximately 1,000 to 2,000×, with built-in scale bars (e.g., 10 μm or 5 μm) used for spatial calibration. EDS was employed to perform point analyses on selected regions to reveal the elemental distribution on the sample surfaces. The analytical precision of EDS ranged from 0.1 to 1 wt%. The statistical standard deviations (sigma) for each element were as follows: O-0.58 wt%, Al-0.20 wt%, Si-0.17 wt%, I-0.60 wt%, Pb-0.73 wt%, Fe-0.21 wt%, Na-0.17 wt%, Mg-0.15 wt%, and K-0.10 wt%. To complement the BSE imaging and provide detailed surface morphological information, SEM imaging in secondary electron (SE) mode (Signal A = SE2) was also performed using the same Zeiss SEM under the same operating conditions (accelerating voltage of 20 kV, WD of approximately 8.5 mm). This mode was used to highlight fine surface features and topographical details of the sample, facilitating the selection of precise regions for further analysis and FIB sectioning. Typical magnifications were set to 1,000×, with spatial calibration achieved using a 10 μm scale bar.

To further investigate the microstructure and composition of the sample, a single electron-transparent thin-foil sample (approximately 90 nm thick) was prepared from the selected region of interest. The thin-foil was fabricated using a FIB-SEM system (FEI Helios NanoLab Dual FIB-SEM). During preparation, a ~1 μm thick Pt protective layer was first deposited on the target microregion to minimize structural damage during the milling process. A high-energy Ga^+ ion beam was then used to excavate two trenches adjacent to the Pt protective layer, gradually exposing the target sample. When approaching the target sample, the ion beam current was reduced for fine milling. The sample was then extracted from the bulk material using a nanomanipulator and welded to a Cu grid with Pt. Finally, a low-energy ion beam was used to further thin the sample to achieve electron transparency (~90 nm thick). Before TEM imaging, the sample was placed in immersion mode to enhance image resolution.

TEM and high-resolution transmission electron microscopy (HRTEM) analyses were performed using an FEI Tecnai G2 F20 TEM operating at an accelerating voltage of 200 kV. The instrument is equipped with an EDS detector (detection limit of ~0.5–1 wt%) for morphological and compositional characterization of the embedded nanoparticles. Selected-area electron diffraction (SAED) was also conducted to determine the crystal structure. Additionally, for higher Z-contrast and ultra-high resolution, some analyses were conducted using a probe-corrected FEI Titan Themis S/TEM in high-angle annular dark-field (HAADF) mode combined with STEM. Using an inner collection angle greater than 50 mrad, sub-Å spatial resolution was achieved, enabling precise characterization of the elemental distributions and phase boundaries. During the TEM-EDS Mapping analysis, the accelerating voltage was set at 200 kV. The image resolution was 1024 × 1024 pixels, and the actual width of the analyzed area was 2000 nm. The acquisition time was adjusted according to the elemental abundances. Polynomial fitting and other algorithms were employed to subtract the X-ray background signal. The energy resolution of the EDS was approximately 136 eV, and the energy calibration error for all rare − earth element Lα spectral lines was controlled within ± 0.05 keV. After data processing, colored elemental distribution maps were generated (for example, Fe-yellow, Mn-magenta, Ti-green). It should be noted that TEM-EDS mapping at the nanoscale is inherently semi-quantitative; therefore, the elemental concentrations and stoichiometric ratios in this study are interpreted as indicative or approximate, and are not intended as strictly quantitative measurements.

For data processing and analysis, HRTEM images were post-processed using DigitalMicrograph® software (Version 3.53.4141.0, Gatan Inc.). This included applying Fast Fourier Transforms (FFT) to generate SAED patterns for crystal orientation determination and lattice spacing measurements. As needed, other data processing software was also employed for analyzing and visualizing elemental mapping data.

3. Results

3.1. The morphology and internal structure of Fe-Mn micronodules

The Fe-Mn micronodules analyzed in this study range in size from approximately 2 to 10 μm (Fig. 2). SEM-EDS analysis (Table 1) indicates that the surface elemental composition of these micronodules includes O (8.87–27.70 wt%), Al (1.29–3.27 wt%), Si (2.49–8.30 wt%), I (29.98–47.24 wt%) and Pb (28.09–39.88 wt%). Among them, micronodule #1 (Fig. 2a) exhibits a loosely packed, irregular morphology, while micronodules #2, #3 and #4 (Fig. 2b, c, A. 1) show spherical or irregular flattened shapes, with colloform-like microstructural protrusions observed on their surfaces (Fig. 2d). Based on this, a more detailed analysis was performed on micronodule #2.

This micronodule contains numerous pores and loosely packed structures but also exhibits a distinct dense core (Fig. 3a, A. 2) composed of elongated columnar particles. Surrounding the core is a relatively compact, layered structure that gradually transitions outward into a porous, loosely packed layer. The outermost surface, however, becomes dense and layered again. Between the dense core and the outermost layer, there exists an intermediate layer with a relatively compact sheet-like structure. Over time, with the stabilization of the depositional environment and continuous precipitation of elements, these micronodules may further develop into typical Fe-Mn nodules with well-defined layering and more regular morphology. In the HAADF image (Fig. 3b), the laminated structures appears prominently bright, attributed to its primary composition of tightly packed elements with larger atomic numbers. Conversely, the loose layers, primarily composed of elements with smaller atomic numbers and exhibiting a relatively loose configuration, results in reduced electron scattering, rendering this region noticeably darker (Xu et al., 2024b). This layered structure not only reflects the complexity of the micronodule but also provides crucial clues for understanding its genesis and compositional distribution.

3.2. Major elements distribution in Fe-Mn micronodules

Fig. 4a illustrates the fundamental distribution characteristics of the major elements within the Fe-Mn micronodule. It shows the distribution of key elements, including Ti, Mn, Fe, I and Pb, which exhibit a distinct layered pattern. In Fig. 4b, the overlapping regions in different colors indicate the distribution of clay minerals, composed primarily of O, Mg, Al, Si and K. The distribution characteristics of these major elements will subsequently be detailed in order, from the core of the micronodule to its

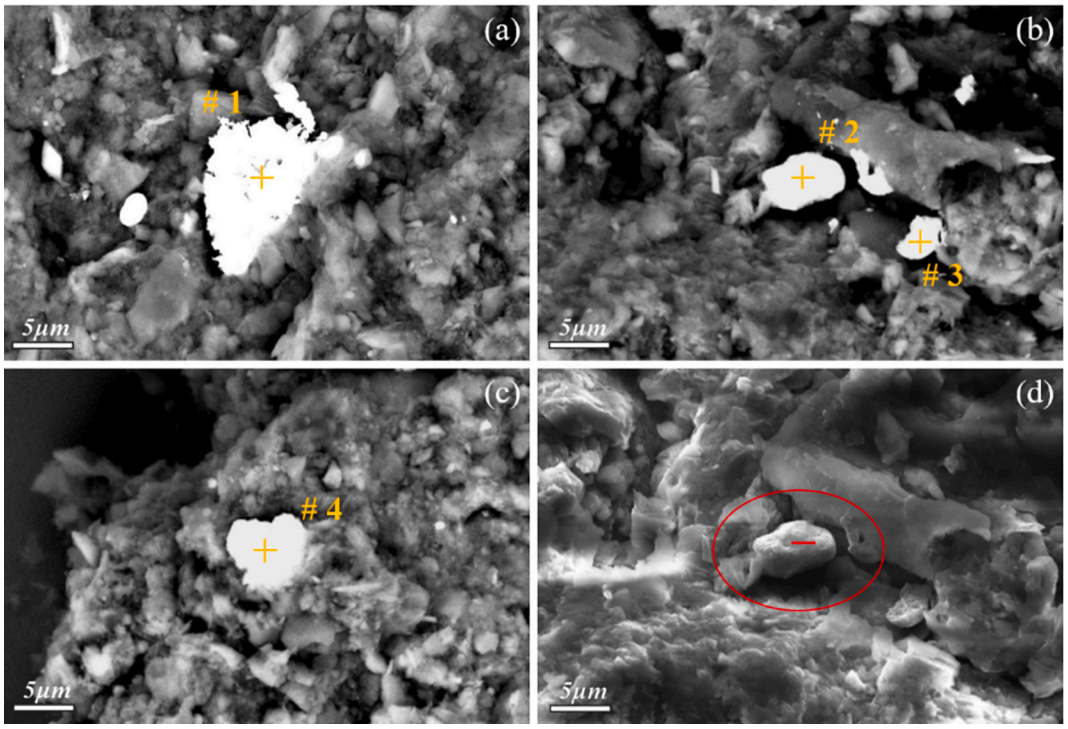

Fig. 2. SEM-BSE images of the Fe-Mn micronodules (a–c) and SEM-SE image of the micronodule selected for FIB sectioning (d). The orange crosses indicate the locations of point analyses, the red circle marks the target micronodule region for further analysis, and the red line denotes the specific location prepared for FIB sectioning. (For interpretation of the references to color in this figure legend, the reader is referred to the web version of this article.)

Table 1
EDS results on the surface of Fe-Mn micronodules samples.

Wt%Point	O	Al	Si	I	Pb	Fe	Na	Mg	K
1	10.35	1.68	3.98	44.05	39.88				
2	8.87	1.29	2.49	47.24	38.63	1.12			
3	14.43	3.27	8.30	36.90	30.33	3.06	0.97	1.12	1.03
4	27.70	2.91	5.98	29.98	28.09	2.68	0.73	1.36	0.38

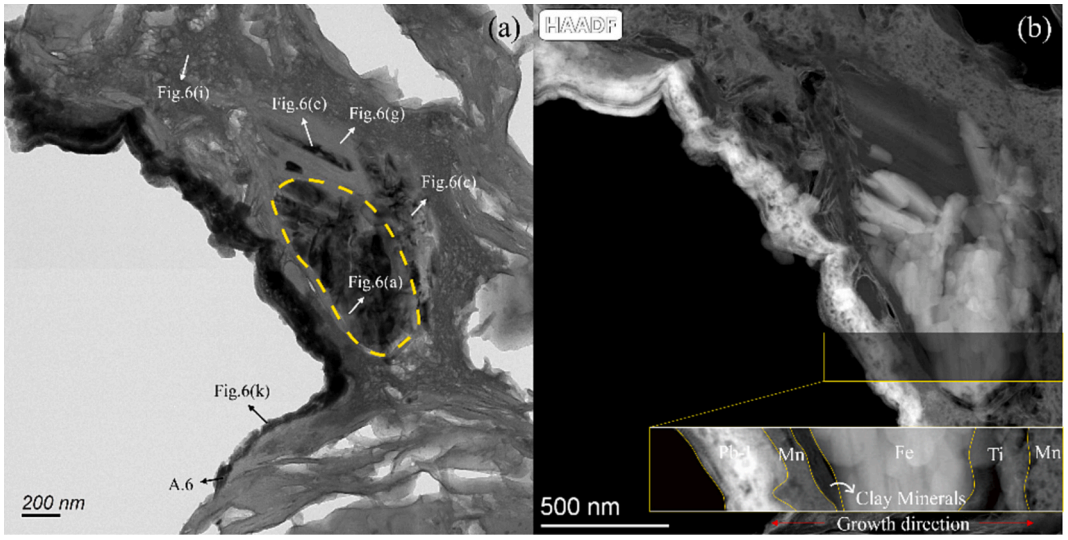

Fig. 3. Fe-Mn micronodule (the dotted line part is the nucleation center) and HAADF electron microscopic image. The sectioning position is located at the red short line in Fig. 2d. (For interpretation of the references to color in this figure legend, the reader is referred to the web version of this article.)

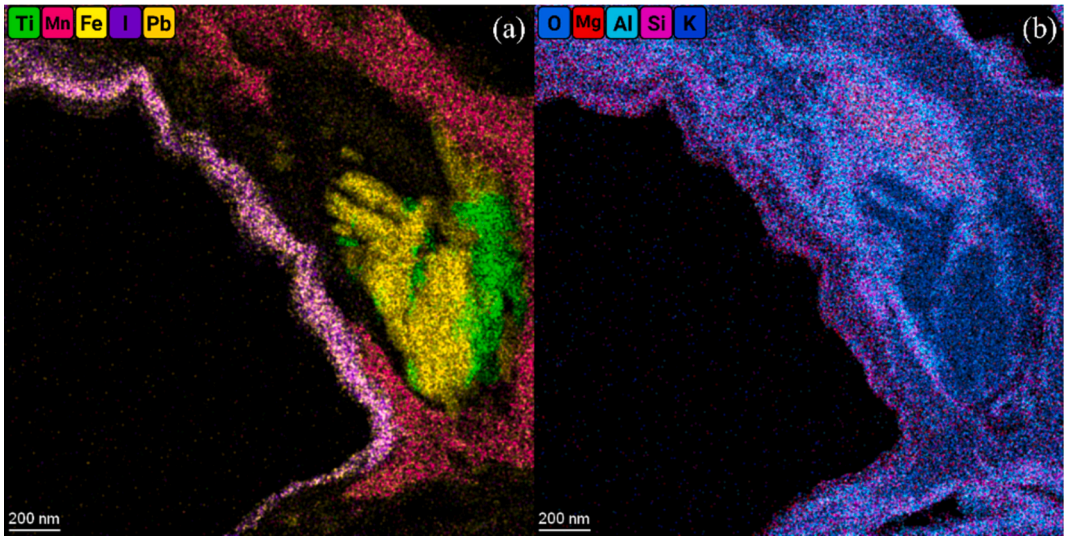

Fig. 4. Color mapping of different chemical compositions in the micro-growth layer inside the Fe-Mn micronodule.

edge.

HAADF observations reveal the presence of elongated columnar nanoparticles in the core of the micronodule. This imaging mode, which highlights regions with higher atomic numbers as brighter areas, provides a clear visualization of density variations in the core (Fig. 3b). TEM-EDS analysis demonstrates that the core region is primarily composed of O, Fe and Ti (Fig. 5a–c). Based on these findings, this study classifies the core of the micronodule into two distinct zones: Fe-rich regions and Ti-rich regions.

In the Fe-rich region of the core, numerous rod-shaped ferrihydrite nanoparticles measuring ~70 nm in length are evident, though their indistinct boundaries preclude precise dimensional measurements (Fig. 3a). According to TEM-EDS imaging (Fig. 5a and b), these nanoparticles primarily comprise O and Fe. High-resolution images (Fig. 6a) reveal a lattice spacing of about 1.09 nm, corresponding to the (0 0 1) plane of ferrihydrite. Meanwhile, the SAED pattern (Fig. 6b) exhibits single-crystal diffraction spots, indicating a monocrystalline nature; however, the limited number of spots suggests that the overall crystallinity remains relatively low.

Fhy- Frrihydrite; Mnt- Montmorillonite.

In the Ti-rich region of the core, rod-shaped titanium oxide nanoparticles can also be clearly observed through HAADF imaging, although their density is lower compared to the Fe-rich region (Fig. 3b). Surface scanning images (Fig. 5a and c) indicate that the primary elements in this region are O and Ti. HRTEM imaging (Fig. 6c) reveals that some nanoparticles exhibit distinct lattice fringes, suggesting a certain degree of crystallinity, albeit with relatively large lattice spacings. The SAED pattern indicates that these nanoparticles possess a single-crystal structure but with relatively low crystallinity (Fig. 6d). Measurements show that the lattice spacing of these titanium oxide nanoparticles is approximately 1.25 nm. Clearly, in the core region of the Fe-Mn micronodule, titanium primarily exists in the form of titanium oxides, closely associated with ferrihydrite, with some titanium distributed along the fractures of ferrihydrite (Fig. 4a). Although it represents a mineral phase, it is tentatively classified as titanium oxide due to the lack of a matching crystal structure in the crystal database.

The core of the micronodule is semi-encased by a relatively thick clay mineral layer composed of elements such as Al, Mg, O, Si and K (Fig. 5a, 5d-5 g), exhibiting a textural distribution. Additionally, trace amounts of Fe and Mn are also present. HRTEM images reveal that these clay minerals are composed of two distinct components (Fig. 3a). Therefore, this study categorizes the clay minerals within the micronodule into two

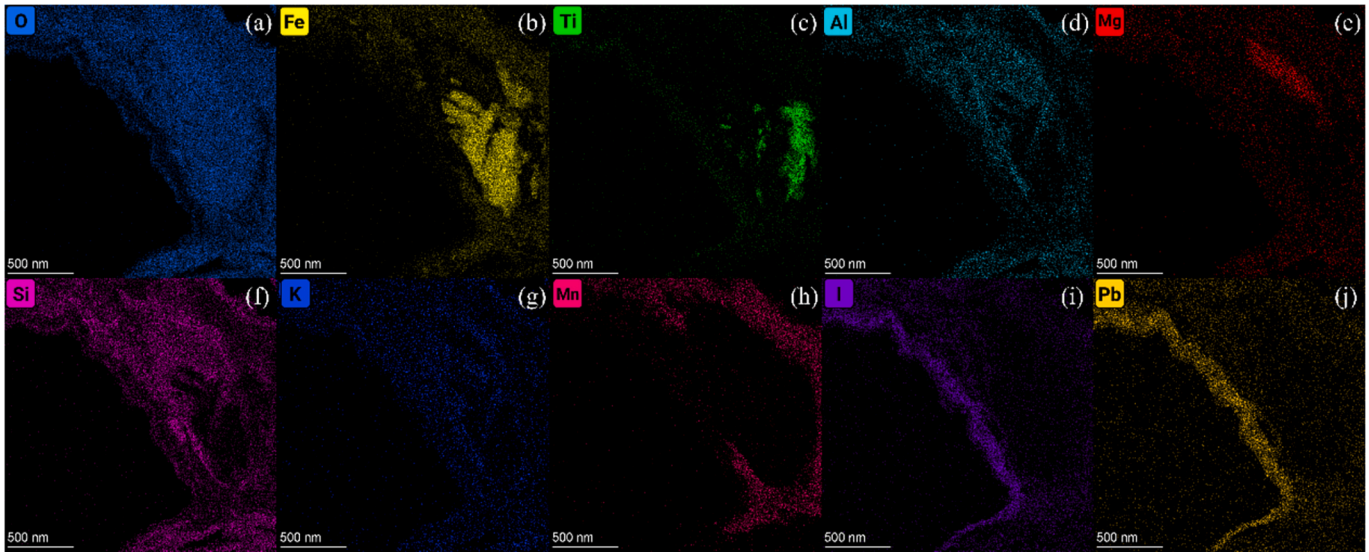

Fig. 5. TEM-EDS color mapping of each element.

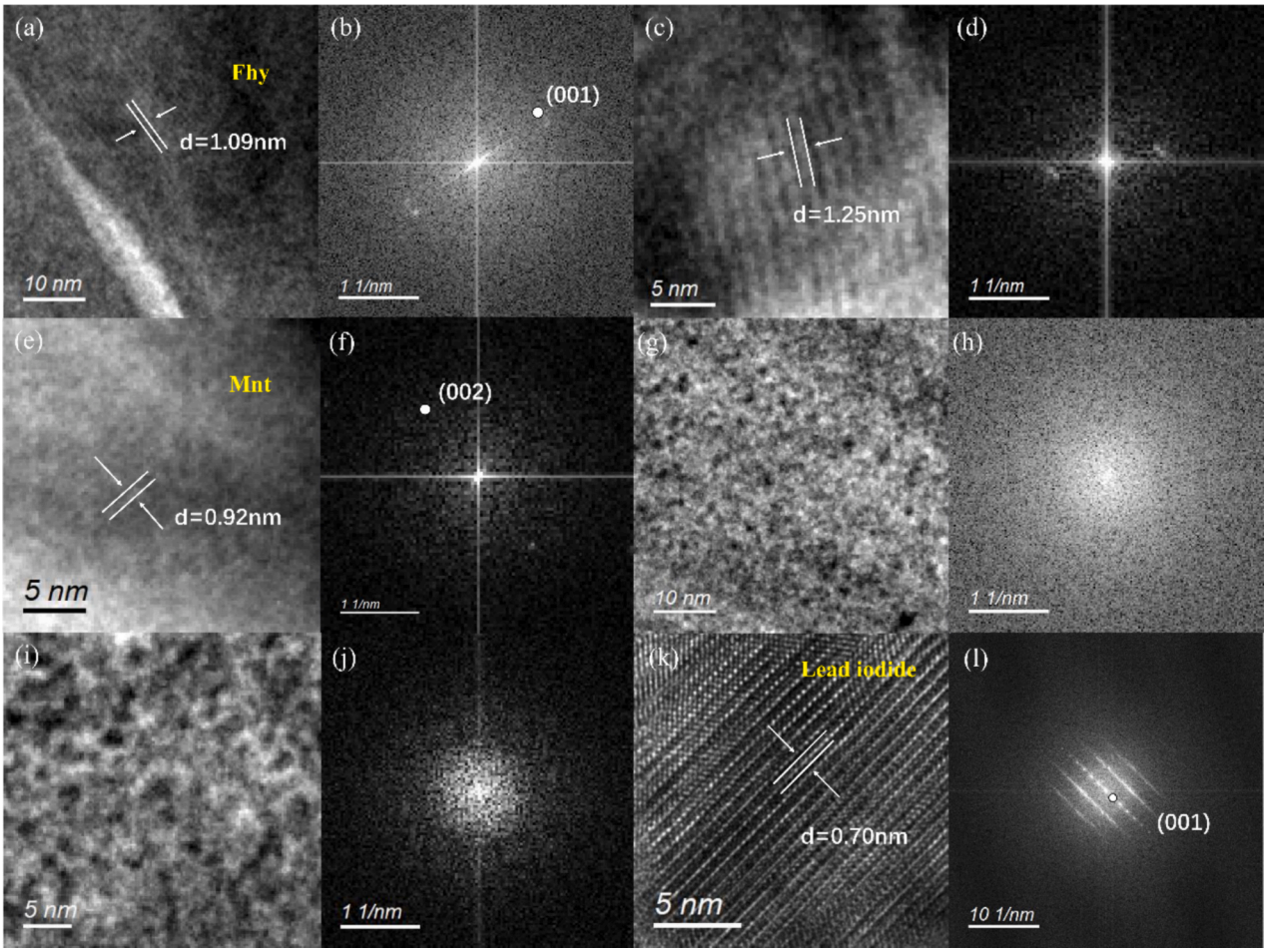

Fig. 6. Interplanar spacing and selected area diffraction pattern of nanoparticles. (a, b) Fe-O. (c, d) Ti-O. (e, f) Mg-Al-O-Si. (g, h) Al-O-Si-K. (i, j) Mn-O. (k, l) Pb-I.

separate components for analysis. The first component consists of montmorillonite nanoparticles, with morphological analysis indicating that these nanoparticles have dimensions of approximately 60 nm (Fig. 3). TEM-EDS analysis (Fig. 5) reveals that these nanoparticles are primarily composed of Mg, Al, O and Si. HRTEM imaging (Fig. 6e) shows relatively large lattice spacings. Furthermore, SAED diffraction analysis (Fig. 6f) indicates that these nanoparticles exhibit a single-crystal structure but with low crystallinity and a relatively disordered atomic arrangement. Further measurements show that the lattice fringe spacing is 0.92 nm, corresponding to the (002) crystal plane of montmorillonite. Morphological analysis also suggests that the second component of the clay minerals adopts a lamellar structure, surrounding the montmorillonite (Fig. 3). TEM-EDS imaging (Fig. 5) indicates that this component is primarily composed of Al, O, Si and K. HRTEM imaging (Fig. 6g) does not reveal distinct lattice fringes, suggesting low crystallinity. Additionally, the SAED pattern (Fig. 6h) does not exhibit well-defined single-crystal or polycrystalline diffraction patterns, indicating that this component is amorphous.

The manganese oxide layer, composed of Mn and O, exhibits a porous and loosely packed structure (Fig. 3a), enveloping the core of the micronodule. This loose layer is likely formed by the initial precipitation of manganese oxides and is closely associated with the early growth process of the micronodule. TEM-EDS analysis (Fig. 5h) reveals a significant decrease in Mn content from the edge to the core, suggesting that this distribution pattern may reflect the stepwise growth process of Fe-Mn micronodules. In HRTEM images, no distinct lattice fringes are observed; however, numerous nanoparticles ranging from 0.5 to 1 nm in size can be identified (Fig. 6i). SAED diffraction pattern analysis (Fig. 6j) does not exhibit any well-defined diffraction features, indicating that these nanoparticles are likely amorphous manganese oxides.

Lead iodide is primarily distributed at the edge of the micronodule, forming a dense laminated structure (Fig. 3). TEM-EDS imaging (Fig. 5) reveals that both iodine and lead are enriched in the dense laminated structure at the micronodule's edge, while only minor amounts are present in other regions. This edge enrichment phenomenon, along with the low oxygen content, reflects the influence of localized chemical environments on the formation of the micronodule. Elemental composition analysis indicates that this phase contains 47.24 % iodine and 38.63 % lead (Table 1; A. 3). HRTEM imaging shows distinct lattice fringes, indicating that this compound exhibits a high degree of crystallinity. SAED patterns display well-defined single-crystal diffraction spots, further confirming its single-crystalline structure (Fig. 6l). Measurements show that the lattice fringe spacing of this compound is 0.70 nm, corresponding to the (0 0 1) plane of PbI_2 (lead iodide), which is consistent with the known lattice parameters of PbI_2. The formation of PbI_2 likely reflects the co-precipitation characteristics of iodine and lead in the dense laminated structure at the micronodule's edge under progressively reducing redox conditions.

3.3. Distribution of REEs in Fe-Mn micronodules

From the TEM-EDS images (Fig. 7), it is visually evident that the enrichment of REEs occurs simultaneously with the growth of the Fe-Mn micronodule. The Fe-Mn micronodule analyzed in this study contains REEs including La, Ce, Pr, Nd, Sm, Eu, Gd, Tb, Dy, Ho, Er, Tm and Yb. The specific distribution of REEs within the micronodule is detailed in Fig. 7, as well as A. 4 and A. 5.

Among LREEs, La is primarily concentrated in the Ti-rich portion of

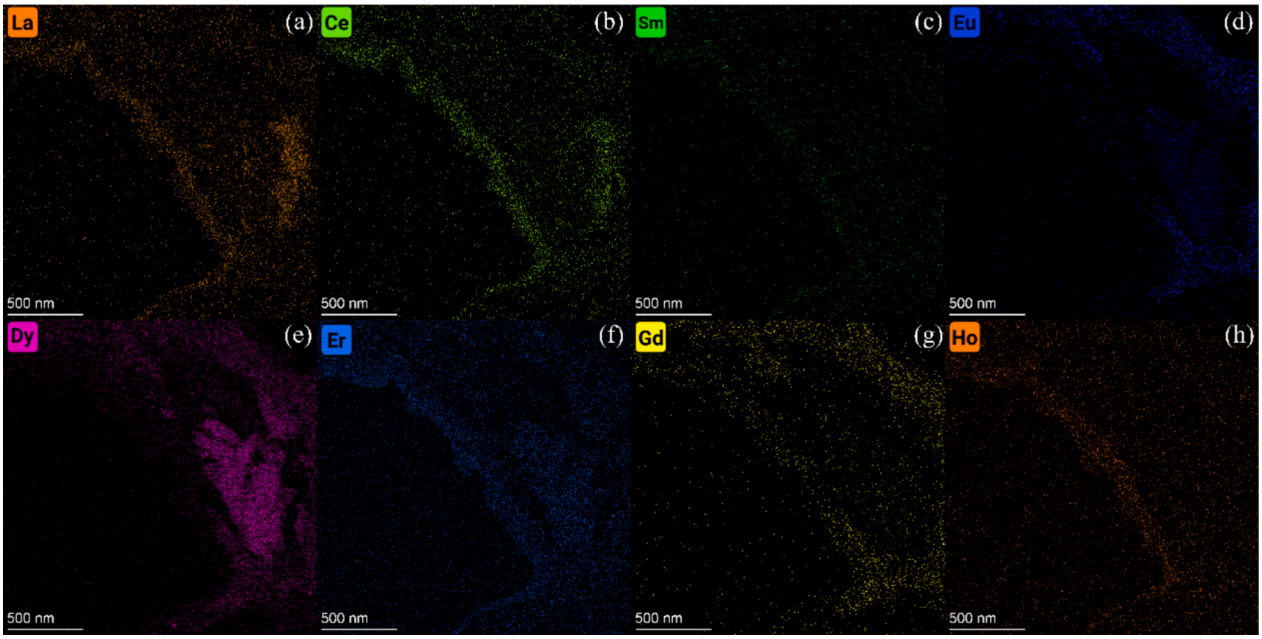

Fig. 7. TEM-EDS color mapping of REEs.

the micronodule's core and in the laminated structures at its edge (Fig. 7; similar to the distribution of Ce and Pr, as shown in A. 4). Sm is primarily enriched in the laminated structures at the edge of the micronodule, similar to Nd. Eu is mainly enriched in the loose layers at the edge of the micronodule, with a width of approximately 250 nm.

Among HREEs, Dy is predominantly concentrated in the Fe-rich portion of the micronodule's core (Fig. 7; similar to Tb, as shown in A. 5). Er is mainly distributed in the Fe-rich portion of the core, a loose layer and the laminated structures at the edge of the micronodule (similar to Tm). Gd is primarily distributed in the loose layers and the laminated structures at the edge of the micronodule. Ho is mainly located in the laminated structures at the edge of the micronodule, a distribution pattern similar to that of Yb.

4. Discussion

4.1. Nanoscale mineralogical characteristics of Fe-Mn micronodules

In the Western Pacific nodules, numerous nanomineral particles dominated by Fe and Mn play a critical role in nodule growth and evolution (Huang et al., 2022). Similarly, in micronodules, these nanoparticles also serve essential functions. To further characterize these particles, we conducted detailed mineralogical analyses using TEM-EDS.

Fig. 6a shows the presence of ferrihydrite, a low temperature, early sedimentary iron oxide nanomineral (Gebauer et al., 2014; Hein et al., 2020), in micronodule #2. Ferrihydrite is typically formed through rapid biotic oxidation of Fe^{2+} or hydrolysis of Fe^{3+} (Wang et al., 2011). It is a poorly crystalline iron hydroxide with small particle size (Liu et al., 2006). In the current micronodule, the ferrihydrite exhibits its characteristic low crystallinity, which aligns with its typical mineralogical properties. Titanium oxide nanoparticles are distributed on the side of the ferrihydrite (Fig. 6c), showing a laminated structure as depicted in Fig. 3a. Furthermore, the clay minerals within the micronodule exhibit a mixed-layer phenomenon and demonstrate increased porosity, as illustrated in Fig. 3a. These findings are similar to previous results by Ju et al. (2016). Fig. 6e depicts montmorillonite within the clay minerals. Previous studies have shown that montmorillonite exhibits a natural nanolayered structure (Wang, 2008) and belongs to nanominerals (Boeva et al., 2016), with fine grain size and low crystallinity (Li and Wang, 2006). Consistent with previous findings, the montmorillonite in the micronodule analyzed in this study exhibits low crystallinity. Although clear lattice fringes are visible in the high-resolution images, the SAED pattern indicates a lack of long-range order, reaffirming its characteristic structural properties. In the composition of nodules, the manganese phase frequently exhibits a very small crystal size and a very low degree of crystallinity, which renders it nearly impossible to identify its complete crystal structure (Qian et al., 2006). Similarly, the nano-scale manganese oxide particles within the micronodule examined in this paper also display an amorphous structure. Lead iodide is not commonly found in nature. Typically, researchers synthesize lead iodide for applications such as the fabrication of perovskite solar cells and other electronic devices (Yang et al., 2015). The lead iodide structure commonly observed in these contexts is in the form of nanosheets (Shkir et al., 2018). However, the lead iodide particles discovered in this study occur naturally and exist in the nanoparticle form (Fig. 3a and k).

FIB-TEM analysis has confirmed that the minerals within the Fe-Mn micronodule in the Western Pacific occur predominantly in the form of nanoparticles. The primary constituents include ferrihydrite, montmorillonite, and lead iodide (all confirmed minerals), along with a poorly crystalline titanium oxides (unmatched to any known mineral) and an amorphous manganese oxides; all components exhibit nanoscale dimensions (Fig. 6c, I and k, A. 6). This indicates that nanoparticles are ubiquitous in primary, non-diagenetic micronodules and further confirms that nanoparticles are an important form of element occurrence in micronodules (Shi et al., 1995; Zhang and Zhou, 2023). The high specific surface area and enhanced surface reactivity of these nanoparticles greatly favor the adsorption and enrichment of metals. Consequently, elucidating the nanoscale characteristics of these minerals is essential for designing efficient extraction or recovery methods for metal resources from Fe-Mn micronodules.

4.2. Element correlation and enrichment characteristics of nano-scale Fe-Mn micronodules

The chemical composition of Fe-Mn nodules is influenced by three critical factors, as suggested in a previous study (Guan et al., 2019): (1) the formation of Fe mineral phases, (2) the formation of Mn mineral phases and (3) the contribution of diagenetic components. Based on elemental correlations, the mineralogical components of the Fe-Mn

micronodule analyzed in this study can be categorized into five groups: (1) ferrihydrite, (2) titanium oxides, (3) clay minerals, (4) manganese oxides and (5) lead iodine. The spatial distribution of elements in the Fe-Mn micronodules, as revealed through these analyses, demonstrates that many elements share similar enrichment patterns.

The REEs in seawater can be absorbed by Fe-Mn nodules through various pathways. Notably, due to electrical property differences, seawater elements are adsorbed onto nodule surfaces via electrostatic interactions. For example, δ-MnO_2 with a strong negative charge preferentially attracts positively charged ions/complexes, while FeOOH's weak positive charge favors negatively charged species (Koschinsky and Hein, 2003; Jiang et al., 2011; Xu and Zhou, 2022). Additionally, certain components within the micronodules may undergo isomorphic substitution with REEs present in seawater. La is mainly concentrated in the laminated structures at the edge of the micronodule associated with I and Pb, and in the Ti-rich core area, a distribution pattern similar to Ce and Pr (Fig. 7a and b, A. 4). As one of the most metallic REEs, La readily forms La^{3+} ions, which can be effectively adsorbed by I^- on the micronodule surface due to strong electrostatic attraction (Wang et al., 2021). The relatively loose structure of manganese oxides provides pathways for La^{3+} to migrate and subsequently be adsorbed by titanium oxides. When the system pH exceeds the point of zero charge (PZC, 6.3) of titanium oxides, these oxides enrich La^{3+} through electrostatic interactions and induce the formation of surface precipitates (Fendorf and Fendorf, 1996). In the sedimentary environment studied here, the pH range is 7.0–7.66 (Lin et al., 2021), which satisfies this adsorption condition. Among the REEs, Ce is particularly notable due to its unique characteristics. In its trivalent state, Ce can be electrostatically attracted to I^- due to differences in electronegativity. Under relatively oxidative conditions, Ce can be oxidized to a tetravalent state (0.87Å), enabling it to undergo isomorphic substitution with Ti^{4+} (0.68Å) in titanium oxides (An et al., 2017). Similarly, Pr in its trivalent state can interact with I^- through electrostatic attraction. Under certain conditions, Pr can transition to a tetravalent state (0.90Å) and undergo isomorphic substitution with Ti^{4+}. While Luo (2023) indicated that anatase primarily adsorbs elements such as La, Ce and Pr, this study demonstrates that the presence of La, Pr and Ce in titanium oxides is not solely due to adsorption; isomorphic substitution is also a significant mechanism for their incorporation. Sm is primarily distributed in the laminated structures at the edge of the micronodule, showing a correlation with the distribution of I and Pb, similar to Nd (Fig. 7c, A. 4). Due to differences in electronegativity, Sm^{3+} can generate electrostatic attraction with I^-. Additionally, under reducing conditions, Sm can readily form Sm^{2+} (1.11Å), which can undergo isomorphic substitution with Pb^{2+} (1.20Å) in lead iodide and can also interact with I^- via electrostatic adsorption. Furthermore, Aliaga et al. (2023) highlighted a close relationship between Pb and Sm, suggesting that the formation of Pb-rich nanocrystals facilitates the enrichment of Sm. Similarly, Nd^{3+} easily undergoes electrostatic adsorption with I^- and remains on its surface. Eu is predominantly distributed in the loose layers within the micronodules and shows a positive correlation with Mn (Fig. 7d). In seawater, Eu tends to form monocarbonate complexes [$REECO_3^+$], which can bind to negatively charged manganese oxides through electrostatic interactions and be adsorbed onto their surfaces (Bau and Koschinsky, 2009; Ohta and Kawabe, 2001; Sheng et al., 2014).

Among HREEs, Dy and Tb within micronodule are mainly distributed in Fe-rich regions of micronodules and show a significant correlation with Fe (Fig. 7e). The ionic radii of Dy^{3+} (0.908 Å) and Tb^{3+} (0.923 Å) have a small difference from that of Fe^{3+} (0.645 Å), allowing their incorporation into the lattice of ferrihydrite through isomorphic substitution (Yang et al., 2021). In a marine setting, Er and Tm typically occur as bis-carbonate complexes [$REE(CO_3)_2^-$], rendering them more easily bound by positively charged ferrihydrite (Fig. 7f, A. 5; Cantrell and Byrne, 1987). Once the redox environment shifts and oxygen availability declines, hydrous iron oxides may undergo partial reduction and dissolve, thereby releasing the previously adsorbed REE^{3+} (Haley et al., 2004). Owing to the negatively charged surfaces and flexible amorphous structures of manganese oxides, those released rare earth ions are subsequently adsorbed and enriched in Mn oxide phases. In addition, the positively charged Er^{3+} and Tm^{3+} can be attracted by I^- through electrostatic forces. In reducing environments, Tm may be reduced to Tm^{2+} (ionic radius 0.94 Å), which can undergo isomorphous substitution with Pb^{2+}. As for Gd, its distribution within the micronodules is mainly concentrated in the outer portion (Fig. 7g). The bicarbonate complex of Gd [$REE(CO_3)_2^-$] can interact with manganese oxides through surface complexation, indicating that the layered structure and high defect density of manganese oxides enrich hydroxyl ligands on their surfaces, which can replace carbonate ligands through ligand exchange reactions (Bau and Koschinsky, 2009). Meanwhile, the electronegativity contrast between Gd^{3+} and I^- can give rise to electrostatic attraction, further influencing Gd's spatial distribution in the micronodules. Ho and Yb share a similar distribution pattern to Sm, being primarily concentrated in the laminated structures at the edge of the micronodule and strongly correlated with I and Pb (Fig. 7h, A. 5). Ho^{3+} can undergo electrostatic attraction with I^-, highlighting the importance of I^- in Ho enrichment. In reducing environments, Yb can exist in the Yb^{2+} state (0.93 Å), allowing it to substitute for Pb^{2+} through isomorphic substitution and adsorb onto I^- through electrostatic attraction. The co-distribution of Yb and Ho in laminated structures indicates that both substitution and adsorption mechanisms play complementary roles in their enrichment.

In addition, surface scanning clearly revealed a strong correlation among Al, Mg, Si and K within the nodules. Higher Mg concentrations were observed in regions with better crystallinity, a phenomenon that can be explained by the promoting effect of Mg on layered silicates (particularly montmorillonite; Harder, 1972). HRTEM analysis further indicates that these elements are enriched in the lamellar structures surrounding the core of the micronodule. Clay minerals, which primarily consist of layered silicates, are characterized by silicon and oxygen forming silicate tetrahedra, with aluminum ions occupying interlayer positions. This structure renders clay minerals highly susceptible to substitution reactions (Zou et al., 2018). For instance, trace amounts of Fe and Mn in the micronodules can replace Al and Mg in clay minerals through isomorphic substitution, thereby incorporating these elements into aluminosilicate minerals (Dai et al., 2018; Jia and Qian, 2020; Wang, 2023). Such substitution reactions are common in clay minerals and represent a key mechanism for their enrichment of other elements. Furthermore, the negatively charged surfaces of clay mineral crystals facilitate the electrostatic adsorption of cations such as K^+ and Mg^{2+} (Li et al., 2022; Zou et al., 2018).

The mechanism of iron-manganese oxides enrichment in REE is primarily attributed to adsorption (Yasukawa et al., 2020). Additionally, analysis results indicate that isomorphic substitution is also an important mechanism contributing to the enrichment of these elements in Fe-Mn micronodules. Early studies have shown that Fe and Mn oxides can capture REEs, with a significantly higher capture efficiency for LREEs than for HREEs (Byrne and Kim, 1990; Koeppenkastrop and De Carlo, 1992; Ohta and Kawabe, 2001). Further research suggests that LREEs in seawater tend to be adsorbed by Mn oxides, while HREEs are more likely to associate with Fe (oxyhydr) oxides (Bau and Koschinsky, 2009; Ohta and Kawabe, 2001). This may be because iron (hydr)oxides have a high specific surface area and surface charge, preferentially adsorbing HREEs with smaller ionic radii through electrostatic interactions. In contrast, LREEs, with relatively larger ionic radii, are more likely to be adsorbed into the interlayer of Mn oxides via cation exchange with interlayer cations (Zhang et al., 2023b). However, the findings of this study reveal some subtle differences. While both Fe (oxyhydr) oxides and Mn oxides are associated with REE enrichment, Fe (oxyhydr) oxides show no significant role in the enrichment of LREEs but exhibit strong positive correlations with HREEs such as Dy, Tb, Er and Tm. In contrast, Mn oxides play a critical role in the accumulation of specific LREE, such as Eu, as well as HREEs, including Er, Tm and Gd. Moreover, Ren et al.

(2019) suggested that vernadite and Fe mineral phases are closely associated with REY enrichment. Guan et al. (2019) noted that the concentrations of Fe, Co, Pb, Ca, Ti, Rb, Sr and REEs are influenced by Fe mineral phases, whereas Mn mineral phases primarily affect the contents of Fe, Si, Ti, Ca, Pb and REEs. Based on a synthesis of previous research findings and the conclusions of this study, we propose that Fe, Mn, Ti, clay minerals, I and Pb collectively serve as key factors driving the enrichment of other elements in marine environments. Titanium oxides play a key role in the enrichment of Ce and Pr in micronodules, while Pb-I influences the enrichment of La, Ce, Pr, Nd, Sm, Gd, Ho, Er, Tm and Yb primarily through electrostatic adsorption and isomorphous substitution.

The microgrowth layers of Fe-Mn micronodules exhibit significantly different chemical compositions, reflecting the enrichment characteristics of elements associated with Fe and Mn minerals (Glasby, 2006). These variations in chemical composition may be closely related to deep-sea depositional processes (Wegorzewski and Kuhn, 2014). Additionally, post-depositional diagenesis in deep-sea sediments can alter the chemical composition of Fe-Mn micronodules, leading to the redistribution or mineralization of manganese (Guan et al., 2019). Notably, due to possible phase transformations of Fe-Mn minerals, previously adsorbed REEs may undergo desorption and redistribution, thereby further increasing the actual contribution of Fe-Mn oxides to elemental enrichment (Liao et al., 2019). Together, these findings clarify which mineral phases act as principal hosts for various REEs in micronodules, thereby providing a fundamental basis for future efforts to quantify REE reserves in marine nodules and to evaluate their resource potential and extractability.

4.3. Early growth process of Fe-Mn micronodules

The formation of Fe-Mn nodules is a continuous process involving complex transformations of material phases (Guan et al., 2019). Previous studies have shown that plagioclase grains, fresh/altered basalts, shark teeth and fish teeth commonly serve as nucleation materials for nodules (Hein et al., 2015; Sensarma et al., 2021). Experimental results from Dou et al. (2012) indicate that when the solution pH exceeds 5.0, Fe^{2+} is rapidly oxidized. As the pH further increases, Fe^{3+} undergoes hydrolysis and progressively polymerizes, leading to the formation of amorphous ferric oxyhydroxides and crystalline compounds. According to Hein et al. (2013), iron in nodules can exist in the form of goethite (α-FeOOH) or lepidocrocite (γ-FeOOH), as well as in an amorphous state dispersed within manganese oxides or in minor amounts as detrital minerals. This study reveals that the core of the observed micronodule is primarily composed of iron minerals, specifically identified as ferrihydrite, with small amounts of iron distributed within the manganese mineral phases (Fig. 8). Following the formation of ferrihydrite, titanium oxides and clay minerals were observed to aggregate on its surface, which is presumed to be related to the strong adsorption capacity of ferrihydrite. The PZC of pure ferrihydrite is approximately 8.0 (Schwertmann and Fechter, 1982). When the environmental pH is slightly below this value, the ferrihydrite surface becomes partially positively charged, facilitating the adsorption of negatively charged clay particles. Notably, the pH in this study area (7.0–7.66) falls within this range. Additionally, the presence of Si on the ferrihydrite surface can reduce its PZC to approximately 5.3–7.0 (Carlson et al., 1981; Schwertmann and Fechter, 1982), making ferrihydrite more negatively charged under slightly alkaline conditions, thereby promoting the adsorption of titanium ions from seawater. As the surface concentration of titanium ions gradually increases and reaches local supersaturation, they may crystallize into titanium oxides, further altering the mineral composition of the core. In terms of redox conditions, the formation of iron minerals generally requires a more oxidizing environment compared to manganese (Guan et al., 2019). As a result, iron tends to precipitate first in environments with relatively high oxidizing conditions, while manganese continues to accumulate in seabed environments with lower oxidation levels (Guan et al., 2019). As Fe-Mn nodules grow in stratified layers, the iron-manganese oxides or detrital minerals enriched in different layers reflect the spatiotemporal fluctuations in redox potential within the depositional environment (Sensarma et al., 2021). This study hypothesizes that the core of these micronodules originated in a relatively oxidizing environment and was subsequently transported to the West Philippine Basin under the influence of LCDW. The combination of a low sedimentation rate and an oxidizing bottom-water environment provides favorable conditions for the formation and growth of Fe-Mn nodules (Cheng et al., 2023). Furthermore, the

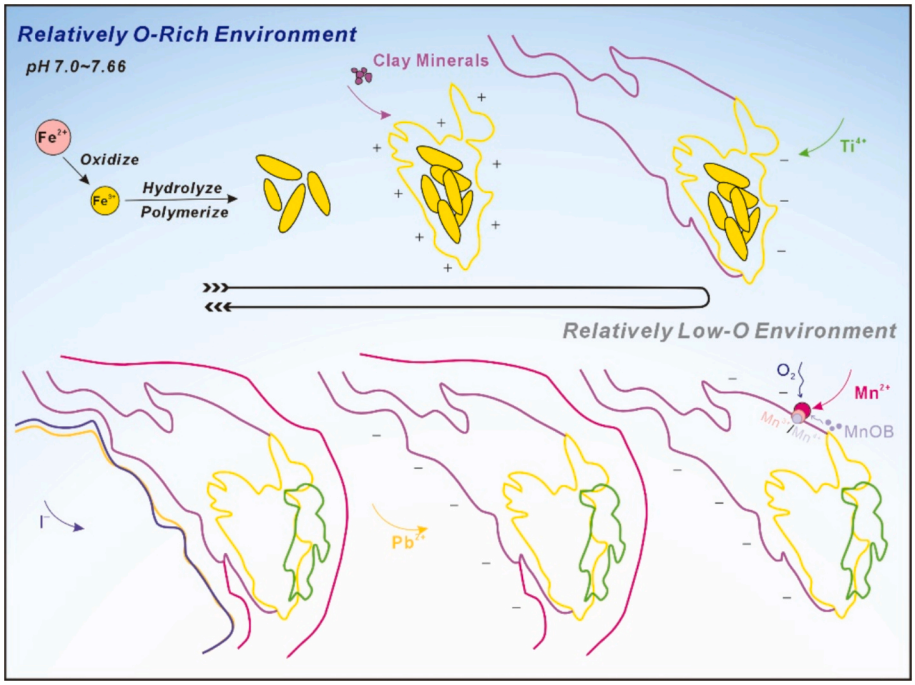

Fig. 8. Schematic diagram of the early formation process of Fe-Mn micronodules.

presence of Fe and Mn lowers the pH at which REEs begin to hydrolyze, making them more likely to precipitate and enrich (Wang et al., 1984).

In deep-sea Fe-Mn micronodules, the clay phase typically consists of montmorillonite and fine-grained quartz (Du and Lv, 2003). In this study, montmorillonite was detected in the clay mineral regions of the micronodule. Due to the small crystal size and low crystallinity of the clay minerals in this region, it was difficult to clearly identify other crystalline phases apart from montmorillonite. However, as shown in Fig. 6g, most of these clay minerals exist as nanoparticles of approximately ~2 nm in size. Fe-Mn nodules in the Pacific Ocean predominantly form in deep-sea clay or siliceous clay environments (Bao, 1991). Once the core of the micronodule is initially formed, large amounts of clay minerals can further facilitate the growth of the micronodule. Additionally, clay minerals carry a negative charge on their surfaces, enabling them to continuously adsorb metal ions such as Pb^{2+} and Mn^{2+} from the surrounding environment. In deep-sea reducing environments, manganese primarily exists in its lower oxidation state (Mn^{2+}), making it highly mobile. When Mn^{2+} interacts with dissolved oxygen supplied from the upper ocean, oxidation reactions occur, gradually forming concentric ring-like structures around a core and simultaneously promoting the hydrolysis of REEs (Wang et al., 1984). Meanwhile, Tebo et al. (2005) noted that manganese-oxidizing bacteria (MnOB) in seawater and deep-sea sediments can further oxidize Mn^{2+} within the nodules to Mn^{3+} or Mn^{4+}. Common manganese mineral phases in Fe-Mn nodules include vernadite, buserite, todorokite and birnessite (Post, 1999; Usui and Someya, 1997; Xu et al., 2024a). From the EDS scanning map (Fig. 4), it can be seen that manganese oxides surround the clay minerals, indicating that manganese enrichment or 'adsorption' likely occurred at a later stage. Under high-resolution imaging (Fig. 6i), it is observed that these manganese oxide grains are approximately 2 nm in size and exhibit poor crystallinity. Similarly, todorokite and birnessite in nature often display characteristics of low crystallinity and small particle size, making their crystal structures challenging to observe.

A layer of lead iodide is observed at the edge of the Fe-Mn micronodule. In polymetallic nodules, Pb is primarily derived from deep-sea precipitation processes. Due to the unique structure and surface charge of manganese oxides, they exhibit a strong adsorption capacity for Pb^{2+} in the environment (Lopes da Costa et al., 2024). Additionally, the surfaces of clay minerals contain numerous active sites capable of stably adsorbing metal ions. In alkaline environments, clay minerals become negatively charged due to the ionization of H^+, thereby enhancing their ability to capture Pb^{2+} and other cations (Pei et al., 2022; Zhang, 2012). When the local concentration of Pb^{2+} in seawater increases, Pb^{2+} preferentially binds to these negatively charged sites, forming stable ionic bonds or inner-sphere complexes, which explains the adsorption of Pb^{2+} onto clay minerals observed in this study. A study by Zhong et al. (2017) on nodules indicated that Pb is primarily associated with Fe-Mn oxide phases. However, the analysis of Fe-Mn micronodules in this study reveals a weaker correlation between Pb and iron, suggesting that Pb is more likely to be associated with clay minerals and manganese oxides. In seawater, iodine primarily exists in the forms of iodate (IO_3^-), iodide (I^-) and elemental iodine (I_2), with iodate (+5 oxidation state) being the most abundant and stable form (Gong and Zhang, 2013). In oxygen-rich alkaline seawater, iodine in the + 5 oxidation state is relatively stable, whereas iodine in the −1 oxidation state exists in a metastable form (Cook et al., 2000; Luther, 2023). However, as the redox potential of manganese is higher than that of iron (Guan et al., 2019), this suggests that the later-stage formation of micronodule occurs in relatively low-oxygen conditions, where iodine predominantly exists in the −1 oxidation state. Additionally, iodine in the + 5 oxidation state can be biologically transformed into the −1 oxidation state (Luther, 2023). During the formation of micronodules, iodine in seawater interacts with the constituents of the micronodules and can be adsorbed or incorporated into their matrices. In this study, a dense and highly crystalline Pb-I layer was observed on the surface of clay minerals. The proposed formation mechanism involves the initial adsorption of Pb^{2+} by the clay minerals, followed by the adsorption of iodate/iodide ions onto the surface at edge variable charge sites or induced by changes in the local microenvironment. This process ultimately leads to the in-situ crystallization of Pb-I compounds (lead iodide) in localized regions. Typically, the direct adsorption capability of clay minerals for anions is relatively weak due to the predominantly negative charge of their layers. However, under neutral or weakly acidic/alkaline conditions, the hydroxyl groups at the edges of clay minerals can become positively charged, enabling electrostatic or complexation adsorption of anions such as I^- and IO_3^-. Furthermore, literature indicates that certain layered silicate clays do exhibit variable charges (Singh et al., 2014), which supports the possibility of Pb and I enrichment and crystallization on the surfaces or within the pores of clay minerals.

The growth mechanism of Fe-Mn nodules is a complex process. The active sites on the nodules surface can adsorb ions from solution, and dissolved substances in seawater may precipitate onto the nodules surface to form solid particles (Li et al., 2024). Additionally, the growth of nodules may involve redox reactions and interactions with other substances. As shown in Fig. 3a, the lead iodide particles attached to the edge of the micronodule surface highlight the range of interaction mechanisms that could be involved in the growth of Fe-Mn nodules. The attachment of lead iodide particles not only demonstrates the adsorption capacity of the micronodule surface but also indicates the potential of nodules to adsorb and fix other substances from seawater. This observation provides valuable insights for further exploration of the formation mechanisms of Fe-Mn micronodules.

5. Conclusions

This study systematically analyzed the internal structure and elemental distribution of Fe-Mn micronodules (early-stage formations) in the deep-sea environment of the Western Pacific. The results reveal that the micronodules exhibit multi-layered growth textures, including dense layers, lamellar structures and porous loose layers. The core of the micronodule is primarily composed of a dense laminated structure rich in Fe and Ti, surrounded by lamellar clay minerals. The outer layer consists of loose layers of manganese oxides, while the edge of the micronodule feature dense layers enriched in iodine and lead. Overall, the distribution of Fe and Mn shows a clear negative correlation. In terms of elemental enrichment, ferrihydrite exhibits a strong correlation with HREEs (e.g., Dy, Tb, Er, Tm), while manganese oxides play a significant role in the enrichment of specific LREE (e.g., Eu) and certain HREEs (e.g., Er, Tm, Gd). Additionally, Ti, clay minerals and locally enriched I and Pb collectively contribute to the synergistic enrichment of various elements at the microscale, such as Tm, Er, Gd, Yb, Ho, Ce, Pr, La, Nd, Sm, K and Mg. The study demonstrates that the constituents within the micronodule, including ferrihydrite, montmorillonite, titanium oxides, manganese oxides and lead iodide, all exist in the form of nanoparticles. The high specific surface area and surface activity of these nanoparticles facilitate the selective enrichment of key metals. These findings indicate that the heterogeneous distribution of microstructure and composition reflects the dynamic changes in redox conditions during sedimentation, underscoring the critical role of nanoparticles in element occurrence and enrichment. Through this study, we not only identified the primary mineral components within the micronodule (e.g., ferrihydrite and montmorillonite) but also uncovered the complex interactions between minerals and compounds at the nanoscale, providing new insights into the genesis and evolution of deep-sea Fe-Mn micronodules and the mechanisms of rare earth element enrichment.

Declaration of competing interest

The authors declare that they have no known competing financial interests or personal relationships that could have appeared to influence the work reported in this paper.

Acknowledgements

This study was financially supported by the National Natural Science Foundation of China (Grant No. 42102076) and the Shandong Provincial Natural Science Foundation (Project No. ZR2021QD037). Furthermore, it received funding from the Spanish Grant NANOMET PID2022-138768OB-I00, funded by MCIN/AEI (https://doi.org/10.13039/50110001133) and co-financed by the European Regional Development Fund (ERDF), "A way of making Europe," under the European Union. Additionally, support was provided by the Sinomate Institute of Materials Research (Guangzhou) Co., Ltd. (SIMR) for assistance with TEM/SEM characterization.

Appendix A. Supplementary data

Supplementary data to this article can be found online at https://doi.org/10.1016/j.oregeorev.2025.106799.

Data availability

No data was used for the research described in the article.

References

Addy, S.K., 1979. Rare earth element patterns in manganese nodules and micronodules from northwest Atlantic. Geochim. Cosmochim. Acta 43, 1105–1115. https://doi.org/10.1016/0016-7037(79)90097-8.

Aliaga, L.C.R., Afonso, C.R.M., Spinelli, J.E., Kiminami, C.S., Bolfarini, C., Botta, W.J., 2023. Advanced characterization of Al–Ni-Sm amorphous alloys with dispersion of round Pb-rich nanoparticles. J. Mater. Res. Technol. 27, 6892–6899. https://doi.org/10.1016/j.jmrt.2023.10.169.

An, D., Luo, X., Xie, Z., Li, T., Liu, P., 2017. Effect of CeO_2 addition on sintering property and microstructure of $CaTiO_3$ ceramics. J. Synth. Cryst. 46, 480–485. https://doi.org/10.16553/j.cnki.issn1000-985x.2017.03.015.

Bao, G., 1991. Study on the dominant factors controlling the geochemical characteristics of iron-manganese nodules——I.Geochemical characteristics of Fe-Mn nodules. Sci. China, Ser. B:Chem. 860–866.

Bau, M., Koschinsky, A., 2009. Oxidative scavenging of cerium on hydrous Fe oxide: evidence from the distribution of rare earth elements and yttrium between Fe oxides and Mn oxides in hydrogenetic ferromanganese crusts. Geochem. J. 43, 37–47. https://doi.org/10.2343/geochemj.1.0005.

Bau, M., Schmidt, K., Koschinsky, A., Hein, J., Kuhn, T., Usui, A., 2014. Discriminating between different genetic types of marine ferro-manganese crusts and nodules based on rare earth elements and yttrium. Chem. Geol. 381, 1–9. https://doi.org/10.1016/j.chemgeo.2014.05.004.

Boeva, N.M., Bocharnikova, Y.I., Belousov, P.E., Zhigarev, V.V., 2016. Determining the cation exchange capacity of montmorillonite by simultaneous thermal analysis method. Russ. J. Phys. Chem. A 90, 1525–1529. https://doi.org/10.1134/S0036024416080057.

Byrne, R.H., Kim, K.-H., 1990. Rare earth element scavenging in seawater. Geochim. Cosmochim. Acta 54, 2645–2656. https://doi.org/10.1016/0016-7037(90)90002-3.

Cantrell, K.J., Byrne, R.H., 1987. Rare earth element complexation by carbonate and oxalate ions. Geochim. Cosmochim. Acta 51, 597–605. https://doi.org/10.1016/0016-7037(87)90072-X.

Carlson, L.T., Schwertmann, U., 1981. Natural ferrihydrites in surface deposits from Finland and their association with silica. Geochim. Cosmochim. Acta 45, 421–429. https://doi.org/10.1016/0016-7037(81)90250-7.

Cheng, Y., Xu, Y., Yi, L., Li, D., Lin, F., Yin, X., Wang, A., 2023. Chronology and critical metals enrichment mechanism of ferromanganese nodules from the Parece Vela Basin. Philippine Sea. Chem. Geol. 630, 121494. https://doi.org/10.1016/j.chemgeo.2023.121494.

Cook, P.L.M., Carpenter, P.D., Butler, E.C.V., 2000. Speciation of dissolved iodine in the waters of a humic-rich estuary. Mar. Chem. 69, 179–192. https://doi.org/10.1016/S0304-4203(99)00104-8.

Dai, H., Wang, D., Liu, L., Huang, F., Wang, C., 2018. Study on emerald-level beryl from the Zhen'an W-Be polymetallic deposit in Shaanxi Province by electron probe microanalyzer and micro X-ray diffractometer. Rock Miner. Anal. 37, 336–345. https://doi.org/10.15898/j.cnki.11-2131/td.201712140193.

Dekov, V.M., Marchig, V., Rajta, I., Uzonyi, I., 2003. Fe-Mn micronodules born in the metalliferous sediments of two spreading centres: the East Pacific rise and Mid-Atlantic Ridge. Mar. Geol. 199, 101–121. https://doi.org/10.1016/S0025-3227(03)00124-5.

Dekov, V.M., Rouxel, O., Guéguen, B., Wegorzewski, A.V., Khripounoff, A., Menot, L., 2021. Mn-micronodules from the sediments of the Clarion-Clipperton zone (Pacific Ocean): origin, elemental source, and Fe-Cu-Zn-isotope composition. Chem. Geol. 580, 120388. https://doi.org/10.1016/j.chemgeo.2021.120388.

Dou, J., Shi, Y., Zhang, W., Li, L., Liu, D., 2012. Influencing factors on removal of trivalent arsenic in raw water by zero-valent iron. Water Purif. Technol. 31, 23–25. https://doi.org/10.15890/j.cnki.jsjs.2012.03.020.

Dubinin, A.V., Sval'nov, V.N., 2000a. Geochemistry of rare earth elements in ferromanganese micro- and macronodules from the Pacific nonproductive zone. Lithol. Min. Resour. 35, 520–537. https://doi.org/10.1023/A:1026693314236.

Dubinin, A.V., Sval'nov, V.N., 2000b. Geochemistry of rare earth elements in micro-and macronodules from the pacific bioproductive zone. Lithol. Min. Resour. 35, 19–31. https://doi.org/10.1007/BF02788282.

Dubinin, A.V., Sval'nov, V.N., Berezhnaya, E.D., Rimskaya-Korsakova, M.N., Demidova, T.P., 2013. Geochemistry of trace and minor elements in sediments and manganese micronodules from the Angola Basin. Lithol. Min. Resour. 48, 175–197. https://doi.org/10.1134/S0024490213030048.

Dubinin, A.V., Uspenskaya, T.Y., Rimskaya-Korsakova, M.N., Demidova, T.P., 2017. Rare elements and Nd and Sr isotopic composition in micronodules from the Brazil Basin, Atlantic Ocean. Lithol. Min. Resour. 52, 81–101. https://doi.org/10.1134/S0024490217020043.

Du, L., Lv, X., 2003. A review of the study on polymetallic nodules in ocean. Geol. Resour. 12, 185–187. https://doi.org/10.13686/j.cnki.dzyzy.2003.03.009.

Fendorf, S., Fendorf, M., 1996. Sorption mechanisms of lanthanum on oxide minerals. Clays and Clay Miner. 44, 220–227. https://doi.org/10.1346/CCMN.1996.0440207.

Gebauer, D., Kellermeier, M., Gale, J.D., Bergström, L., Cölfen, H., 2014. Pre-nucleation clusters as solute precursors in crystallisation. Chem. Soc. Rev. 43, 2348–2371. https://doi.org/10.1039/c3cs60451a.

Glasby, G.P., 2006. Manganese: Predominant role of nodules and crusts. In: Schulz, H.D., Zabel, M. (Eds.), Marine Geochemistry, Second Revised, Updated and, extended edition. Springer, Berlin Heidelberg New York, pp. 371–415.

Glasby, G.P., Keays, R.R., Rankin, P.C., 1978. The distribution of rare earth, precious metal and other trace elements in recent and fossil deep-sea manganese nodules. Geochem. J. 12, 229–243. https://doi.org/10.2343/geochemj.12.229.

Gong, T., Zhang, X., 2013. Determination of iodide, iodate and organo-iodine in waters with a new total organic iodine measurement approach. Water Res. 47, 6660–6669. https://doi.org/10.1016/j.watres.2013.08.039.

Guan, Y., Ren, Y., Sun, X., Xiao, Z., Wu, Z., Liao, J., Guo, Z., Wang, Y., Huang, Y., 2019. Fine scale study of major and trace elements in the Fe-Mn nodules from the South China Sea and their metallogenic constraints. Mar. Geol. 416, 105978. https://doi.org/10.1016/j.margeo.2019.105978.

Guan, Y., Sun, X., Ren, Y., Jiang, X., 2017. Mineralogy, geochemistry and genesis of the polymetallic crusts and nodules from the South China Sea. Ore Geol. Rev. 89, 206–227. https://doi.org/10.1016/j.oregeorev.2017.06.020.

Halbach, P., Scherhag, C., Hebisch, U., Marchig, V., 1981. Geochemical and mineralogical control of different genetic types of deep-sea nodules from the Pacific Ocean. Miner. Deposita 16, 59–84. https://doi.org/10.1007/BF00206455.

Haley, B.A., Klinkhammer, G.P., McManus, J., 2004. Rare earth elements in pore waters of marine sediments. Geochim. Cosmochim. Acta 68, 1265–1279. https://doi.org/10.1016/j.gca.2003.09.012.

Harder, H., 1972. The role of magnesium in the formation of smectite minerals. Chem. Geol. 10, 31–39. https://doi.org/10.1016/0009-2541(72)90075-7.

Hein, J.R., Koschinsky, A., 2013. Deep-ocean ferromanganese crusts and nodules, 2nd ed, Treatise on Geochemistry: Second Edition. Published by Elsevier Inc. https://doi.org/10.1016/B978-0-08-095975-7.01111-6.

Hein, J.R., Koschinsky, A., Kuhn, T., 2020. Deep-ocean polymetallic nodules as a resource for critical materials. Nat. Rev. Earth Environ. 1, 158–169. https://doi.org/10.1038/s43017-020-0027-0.

Hein, J.R., Mizell, K., Koschinsky, A., Conrad, T.A., 2013. Deep-ocean mineral deposits as a source of critical metals for high- and green-technology applications: comparison with land-based resources. Ore Geol. Rev. 51, 1–14. https://doi.org/10.1016/j.oregeorev.2012.12.001.

Hein, J.R., Spinardi, F., Okamoto, N., Mizell, K., Thorburn, D., Tawake, A., 2015. Critical metals in manganese nodules from the Cook Islands EEZ, abundances and distributions. Ore Geol. Rev. 68, 97–116. https://doi.org/10.1016/j.oregeorev.2014.12.011.

Hu, B., Yi, L., Zhao, J., Guo, J., Ding, X., Wang, F., Chen, W., 2021. Magnetostratigraphy of core XT06 and Quaternary sedimentary dynamics of the deep-sea deposits in the West Philippian Basin. Mar. Geol. Quat. Geol. 41, 61–74. https://doi.org/10.16562/j.cnki.0256-1492.2020101301.

Huang, Q.T., He, B., Cai, Z., Huang, Q.R., 2022. The significance of nanomineral particles during the growth process of polymetallic nodules in the western pacific ocean. Int J Env. Res Public Health 19, 13972. https://doi.org/10.3390/ijerph192113972.

Jia, Y., Qian, J., 2020. Study on REE distribution and mineralogical characteristics of different garnets by electron probe and inductively coupled plasma-mass spectrometry. Rock Miner. Anal. 39, 886–895. https://doi.org/10.15898/j.cnki.11-2131/td.202005060007.

Jiang, X., Lin, X., Yao, D., Guo, W., 2011. Enrichment mechanisms of rare earth elements in marine hydrogenic ferromanganese crusts. Sci. China Earth Sci. 54, 197–203. https://doi.org/10.1007/s11430-010-4070-4.

Ju, Y., Sun, Y., Wan, Q., Lu, S., He, H., 2016. Nanogeology: a revolutionary challenge in geosciences. Bull. Mineral. Petrol. Geochem. 35. https://doi.org/10.3969/j.issn.1007-2802.2016.01.001.

Kato, Y., Fujinaga, K., Nakamura, K., Takaya, Y., Kitamura, K., Ohta, J., Toda, R., Nakashima, T., Iwamori, H., 2011. Deep-sea mud in the Pacific Ocean as a potential resource for rare-earth elements. Nat. Geosci. 4, 535–539. https://doi.org/10.1038/ngeo1185.

Kawabe, M., Fujio, S., 2010. Pacific ocean circulation based on observation. J. Oceanogr. 66, 389–403. https://doi.org/10.1007/s10872-010-0034-8.

Koeppenkastrop, D., De Carlo, E.H., 1992. Sorption of rare-earth elements from seawater onto synthetic mineral particles: an experimental approach. Chem. Geol. 95, 251–263. https://doi.org/10.1016/0009-2541(92)90015-W.

Koschinsky, A., Hein, J.R., 2003. Uptake of elements from seawater by ferromanganese crusts: solid-phase associations and seawater speciation. Mar. Geol. 198, 331–351. https://doi.org/10.1016/S0025-3227(03)00122-1.

Lee, S., Xu, H., Xu, W., Sun, X., 2019. The structure and crystal chemistry of vernadite in ferromanganese crusts. Acta Crystallogr., Sect. B:Struct. Sci. Cryst. Eng. Mater. 75, 591–598. https://doi.org/10.1107/S2052520619006528.

Liao, J., Sun, X., Wu, Z., Sa, R., Guan, Y., Lu, Y., Li, D., Liu, Y., Deng, Y., Pan, Y., 2019. Fe-Mn (oxyhydr) oxides as an indicator of REY enrichment in deep-sea sediments from the central North Pacific. Ore Geol. Rev. 112. https://doi.org/10.1016/j.oregeorev.2019.103044.

Lin, G., Huang, J., Lu, J., Su, M., Hu, B., Lin, X., 2021. Geochemical and microbial insights into vertical distributions of genetic potential of N-cycling processes in deep-sea sediments. Ecol. Ind. 125. https://doi.org/10.1016/j.ecolind.2021.107461.

Li, R., Li, X., Li, H., Zhao, K., Peng, K., 2022. Structural characteristics of clay minerals and their progress in CO_2 adsorption. Bull. Chin. Ceram. Soc. 41, 141–152. https://doi.org/10.16552/j.cnki.issn1001-1625.2022.01.008.

Liu, G., Debnath, S., Paul, K.W., Han, W., Hausner, D.B., Hosein, H.-A., Michel, F.M., Parise, J.B., Sparks, D.L., Strongin, D.R., 2006. Characterization and surface reactivity of ferrihydrite nanoparticles assembled in ferritin. Langmuir 22, 9313–9321. https://doi.org/10.1021/la0602214.

Li, X., Wang, Y., 2006. The progress of research on montmorillonite purification. Rock Miner. Anal. 25, 252–258.

Li, Y., Feng, Y., Li, H., Yao, Y., Xu, C., Ju, J., Ma, R., Wang, H., Jiang, S., 2024. Adsorption of metal ions by oceanic manganese nodule and deep-sea sediment: Behaviour, mechanism and evaluation. Sci. Total Environ. 908, 168163. https://doi.org/10.1016/j.scitotenv.2023.168163.

Lopes da Costa, M.A.J., Costa, M.F., Sorrentino, R., Carvalho, N.M.F., de Gois, J.S., 2024. A new approach for the determination of As, Cu, and Pb in seawater samples using manganese oxide octahedral molecular sieve as a sorbent for dispersive solid-phase microextraction. Talanta 268. https://doi.org/10.1016/j.talanta.2023.125320.

Luo, C., 2023. Study on the formation mechanism of the aluminum-bearing rock series in the Jiujialu Formation, central Guizhou. PhD Thesis, Guizhou University. https://doi.org/10.27047/d.cnki.ggudu.2023.000019.

Luo, S., Ren, J., He, G., Deng, X., 2023. Geochemical characteristics of polymetallic nodules and adjacent sediments in the western Pacific Ocean: effects of sedimentary environments on nodules. Mar. Geol. Quat. Geol. 43, 119–135. https://doi.org/10.16562/j.cnki.0256-1492.2022122401.

Luther, G.W., 2023. Review on the physical chemistry of iodine transformations in the oceans. Front. Mar. Sci. 10, 1–16. https://doi.org/10.3389/fmars.2023.1085618.

Menendez, A., James, R.H., Roberts, S., Peel, K., Connelly, D., 2017. Controls on the distribution of rare earth elements in deep-sea sediments in the North Atlantic Ocean. Ore Geol. Rev. 87, 100–113. https://doi.org/10.1016/j.oregeorev.2016.09.036.

Mohtar, A.T., Hughen, K.A., Goodkin, N.F., Streanga, I.M., Ramos, R.D., Samanta, D., Cervino, J., Switzer, A.D., 2021. Coral-based proxy calibrations constrain ENSO-driven sea surface temperature and salinity gradients in the Western Pacific Warm Pool. Palaeogeogr. Palaeoclimatol. Palaeoecol. 561, 110037. https://doi.org/10.1016/j.palaeo.2020.110037.

Niu, J., 2002. Research and development of oceanic multi-metal nodule. China's Manganese Ind. 20, 23–29. https://doi.org/10.14101/j.cnki.issn.1002-4336.2002.02.006.

Ohta, A., Ishii, S., Sakakibara, M., Mizuno, A., Kawabe, I., 1999. Systematic correlation of the Ce anomaly with the Co/(Ni+Cu) ratio and Y fractionation from Ho in distinct types of Pacific deep-sea nodules. Geochem. J. 33, 399–417. https://doi.org/10.2343/geochemj.33.399.

Ohta, A., Kawabe, I., 2001. REE(III) adsorption onto Mn dioxide (δ-MnO_2) and Fe oxyhydroxide: Ce(III) oxidation by δ-MnO_2. Geochim. Cosmochim. Acta 65, 695–703. https://doi.org/10.1016/S0016-7037(00)00578-0.

Pei, Y., Zhang, S., Fang, X., Chen, Y., Zhang, S., Shao, M., Lei, T., 2022. Relationship between metallic elements and organic matter enrichment in self-margin seas: example from surface sediments in the South Yellow Sea. Acta Sedimentol. Sin. 40, 136–148. https://doi.org/10.14027/j.issn.1000-0550.2020.082.

Post, J.E., 1999. Manganese oxide minerals: crystal structures and economic and environmental significance. PNAS 96, 3447–3454. https://doi.org/10.1073/pnas.96.7.3447.

Qian, J., Chu, F., Feng, X., 2006. The main manganates in the polymetallic nodules and their correlations. Acta. Mineral. Sin. 26, 152–158. https://doi.org/10.16461/j.cnki.1000-4734.2006.02.006.

Qiu, X., Li, T., Chang, F., Nan, Q., Xiong, Z., Sun, H., 2014. Sea surface temperature and salinity reconstruction based on stable isotopes and Mg/Ca of planktonic foraminifera in the western Pacific Warm Pool during the last 155 ka. Chin. J. Oceanol. Limnol. 32, 187–200. https://doi.org/10.1007/s00343-014-3073-y.

Ren, Y., Guan, Y., Sun, X., Xu, L., Xiao, Z., Deng, Y., He, W., 2023. Nano-mineralogy and growth environment of Fe-Mn polymetallic crusts and nodules from the South China Sea. Front. Mar. Sci. 10, 1–16. https://doi.org/10.3389/fmars.2023.1141926.

Ren, Y., Sun, X., Guan, Y., Xiao, Z., Liu, Y., Liao, J., Guo, Z., 2019. Distribution of rare earth elements plus yttrium among major mineral phases of marine Fe–Mn crusts from the South China Sea and western Pacific Ocean: a comparative study. Minerals 9, 1–19. https://doi.org/10.3390/min9010008.

Schwertmann, U., Fechter, H., 1982. The point of zero charge of natural and synthetic ferrihydrites and its relation to adsorbed silicate. Clay Miner. 17, 471–476. https://doi.org/10.1180/claymin.1982.017.4.10.

Sensarma, S., Saha, A., Hazra, A., 2021. Implications of REE incorporation and host sediment influence on the origin and growth processes of ferromanganese nodules from Central Indian Ocean Basin. Geosci. Front. 12, 101123. https://doi.org/10.1016/j.gsf.2020.11.017.

Sheng, G.D., Yang, S.T., Li, Y.M., Gao, X., Huang, Y.Y., Hu, J., Wang, X.K., 2014. Retention mechanisms and microstructure of Eu(III) on manganese dioxide studied by batch and high resolution EXAFS technique. Radiochim. Acta 102, 155–167. https://doi.org/10.1515/ract-2014-2088.

Shi, N., Ma, Z., He, W., 1995. Nano-solids in manganese nodules from northern part of Pacific ocean floor. Sci. China Ser. B: Chem. 38, 1493–1500.

Shkir, M., Yahia, I.S., Ganesh, V., Bitla, Y., Ashraf, I.M., Kaushik, A., AlFaify, S., 2018. A facile synthesis of Au-nanoparticles decorated PbI_2 single crystalline nanosheets for optoelectronic device applications. Sci. Rep. 8, 13806. https://doi.org/10.1038/s41598-018-32038-5.

Singh, B., Cattle, S.R., Field, D.J., 2014. Edaphic soil science, introduction to. In: Van Alfen, N.K. (Ed.), Encyclopedia of Agriculture and Food Systems. Academic Press, Oxford, pp. 35–58. https://doi.org/10.1016/B978-0-444-52512-3.00092-9.

Tebo, B.M., Johnson, H.A., McCarthy, J.K., Templeton, A.S., 2005. Geomicrobiology of manganese(II) oxidation. Trends Microbiol. 13, 421–428. https://doi.org/10.1016/j.tim.2005.07.009.

Usui, A., Someya, M., 1997. Distribution and composition of marine hydrogenetic and hydrothermal manganese deposits in the northwest Pacific. Geol. Soc. Spec. Publ. 119, 177–198. https://doi.org/10.1144/GSL.SP.1997.119.01.12.

USCGS, 2013. NOAA/NOS and USCGS Seabed Descriptions from Hydrographic Surveys. https://doi.org/10.7289/V5BG2KWG.

Von Stackelberg, U., 1997. Growth history of manganese nodules and crusts of the Peru Basin. Geol. Soc. Lond. Spec. Publ. 119, 153–176. https://doi.org/10.1144/GSL.SP.1997.119.01.11.

Wang, H., 2008. Study on nano-silver and silver loaded nano-antimicrobial. PhD Thesis, Huazhong University of Science and Technology. https://doi.org/10.7666/d.d048528.

Wang, J., Ma, Y., Feng, W., Gao, N., 2021. Influence of Si/Al ratio on La-loaded fly ash based porous ceramics. J. Mater. Sci. Eng 39, 994–998. https://doi.org/10.14136/j.cnki.issn1673-2812.2021.06.019.

Wang, X., 2023. Study on phase transformation behavior of aluminasilica phase during biomass hydrothermal calcification reduction of high-iron red mud. Master's Thesis, University of Science and Technology Liaoning. https://doi.org/10.26923/d.cnki.gasgc.2023.000465.

Wang, X., Chen, Y., Wu, M., 1984. Geochemistry of RE and trace elements in ferromanganese nodules and their genesis. Oceanol. Limnol. Sin. 15, 501–514.

Wang, X., Yang, K., Sun, S., Xu, J., Li, Y., Liu, F., Feng, X., 2011. The structure and composition of ferrihydrite and its environmental geochemical behaviors. Earth Sci. Front. 18, 339–347.

Wan, S., Yu, Z., Clift, P.D., Sun, H., Li, A., Li, T., 2012. History of Asian eolian input to the West Philippine Sea over the last one million years. Palaeogeogr., Palaeoclimatol. Palaeoecol. 326–328, 152–159. https://doi.org/10.1016/j.palaeo.2012.02.015.

Wegorzewski, A.V., Kuhn, T., 2014. The influence of suboxic diagenesis on the formation of manganese nodules in the Clarion Clipperton nodule belt of the Pacific Ocean. Mar. Geol. 357, 123–138. https://doi.org/10.1016/j.margeo.2014.07.004.

Winter, B.L., Johnson, C.M., Clark, D.L., 1997. Geochemical constraints on the formation of late Cenozoic ferromanganese micronodules from the central Arctic Ocean. Mar. Geol. 138, 149–169. https://doi.org/10.1016/S0025-3227(97)00013-3.

Wu, H., Ge, C., Cai, Y., Shi, X., Huang, M., 2022. Structure, composition, and formation of ferromanganese micronodules at the eastern southwest Indian ridge. Mar. Geol. 451, 106874. https://doi.org/10.1016/j.margeo.2022.106874.

Xu, L., Deng, Y., Guan, Y., Sun, X., Li, D., He, W., Ren, Y., Xiao, Z., 2024a. Nano-mineralogy and mineralization of the polymetallic nodules from the interbasin of seamounts, the western Pacific Ocean. Minerals 14, 1–20. https://doi.org/10.3390/min14010047.

Xu, Y., Song, W., Dai, J., Xue, S., Chen, Q., Yang, J., Xu, D., 2024b. Application progress on transmission electron microscopy in the research of rare earth deposits. Rock Miner. Anal. 43, 641–658. https://doi.org/10.15898/j.ykcs.202402260020.

Xu, Y., Zhou, H., 2022. The elements phase associations of ferromanganese nodules in the seamounts of the South China Sea. Mar. Geol. Front. 38, 20–31. https://doi.org/10.16028/j.1009-2722.2021.146.

Yang, L., Zuo, Z., Yu, F., Ji, S., Wang, T., Wang, M., 2015. Research progress of perovskite solar cells. Technol. Dev. Chem. Ind. 44, 40–45. https://doi.org/10.3969/j.issn.1671-9905.2015.09.011.

Yang, M., Liang, X., Li, Y., He, H., Zhu, R., Arai, Y., 2021. Ferrihydrite transformation impacted by adsorption and structural incorporation of rare earth elements. ACS Earth Space Chem. 5, 2768–2777. https://doi.org/10.1021/acsearthspacechem.1c00159.

Yan, X., Ho, C., Zheng, Q., Klemas, V., 1992. Temperature and size variabilities of the western Pacific warm pool. Sci. 258, 1643–1645. https://doi.org/10.1126/science.258.5088.1643.

Yasukawa, K., Kino, S., Azami, K., Tanaka, E., Mimura, K., Ohta, J., Fujinaga, K., Nakamura, K., Kato, Y., 2020. Geochemical features of Fe-Mn micronodules in deep-sea sediments of the western North Pacific Ocean: potential for co-product metal extraction from REY-rich mud. Ore Geol. Rev. 127, 103805. https://doi.org/10.1016/j.oregeorev.2020.103805.

Yin, Z., Wang, H., Han, J., Lv, X., Shen, Z., Chen, J., He, H., Xie, A., Guan, Y., Dong, C., 2019. Comparison between the marginal-sea polymetallic nodules in the South China Sea and ocean polymetallic nodules. J. Jilin Univ. Earth Sci. Ed. 49, 261–277. https://doi.org/10.13278/j.cnki.jjuese.20180133.

Zhang, H., Zhou, J., Yuan, P., Dong, Y., Fan, W., Chu, F., Xiao, W., Liu, D., 2023a. Highly positive Ce anomalies of hydrogenetic ferromanganese micronodules from abyssal basins in the NW and NE Pacific: implications for REY migration and enrichment in deep-sea sediments. Ore Geol. Rev. 154, 105324. https://doi.org/10.1016/j.oregeorev.2023.105324.

Zhang, L., 2012. Adsorption behaviors of heavy metal Pb (II) on clay minerals. Master's Thesis, Dalian University of Technology.
Zhang, W., Liu, Y., Zhao, W., 2023b. Occurrence and enrichment of cobalt in ferromanganese nodules from the Western Pacific. Ore Geol. Rev. 163, 105758. https://doi.org/10.1016/j.oregeorev.2023.105758.
Zhang, W., Zhou, H., 2023. Research progress on the nanogenesis of hydrogenetic Fe-Mn mineralization. Adv. Earth Sci. 38, 904–915. https://doi.org/10.11867/j.issn.1001-8166.2023.054.
Zhong, Y., Chen, Z., Mo, A., Luo, Y., Li, G., Zheng, X., 2017. Genetic types and elemental occurrence phases of ferromanganese nodules in the northern South China Sea. J. Trop. Oceanogr. 36, 48–59. https://doi.org/10.11978/2016060.
Zou, Y., Zhang, R., Chen, J., Wang, L., Lu, D., 2018. Research advance in the application of clay minerals to phosphorus pollution control in eutrophic water bodies and sediments. Adv. Earth Sci. 33, 578–589. https://doi.org/10.11867/j.issn.1001-8166.2018.06.0578.